論文 / 著書情報
Article / Book Information

Title	Radial dependence diagnosis of inductively coupled Ar plasma based upon optical emission spectroscopic measurement with spectral reflectance compensation
Authors	Yuya Yamashita, Kenta Doi, Tetsuji Kiyota, Keiichiro Asakawa, Sotaro Hosoya, Wataru Kikuchi, Atsushi Nezu, Hiroshi Akatsuka
Citation	Review of Scientific Instruments, Vol. 94, Issue 8, 083503
Pub. date	2023, 8
DOI	https://dx.doi.org/10.1063/5.0138912
note	This article may be downloaded for personal use only. Any other use requires prior permission of the author and AIP Publishing. This article appeared in Yuya Yamashita et al., Rev. Sci. Instrum., 94, 083503,(2023) and may be found at https://doi.org/10.1063/5.0138912

Review of
Scientific Instruments

ARTICLE

pubs.aip.org/aip/rsi

Radial dependence diagnosis of inductively coupled Ar plasma based upon optical emission spectroscopic measurement with spectral reflectance compensation

Cite as: Rev. Sci. Instrum. 94, 083503 (2023); doi: 10.1063/5.0138912
Submitted: 15 December 2022 • Accepted: 19 July 2023 •
Published Online: 9 August 2023

View Online Export Citation CrossMark

Yuya Yamashita,[1,a)] Kenta Doi,[2] Tetsuji Kiyota,[3] Keiichiro Asakawa,[2] Sotaro Hosoya,[1] Wataru Kikuchi,[1] Atsushi Nezu,[4,5] and Hiroshi Akatsuka[1,5]

AFFILIATIONS

[1] Department of Electrical and Electronic Engineering, School of Engineering, Tokyo Institute of Technology, 2-12-1-N1-10 Ookayama, Meguro-ku, Tokyo 152-8550, Japan
[2] Institute of Advanced Technology, ULVAC, Inc., 1220-1 Suyama, Susono-shi, Shizuoka 410-1231, Japan
[3] Strategic Planning Department, ULVAC, Inc., 2500 Hagisono, Chigasaki-shi, Kanagawa 253-8543, Japan
[4] Safety and Radiation Management Division, Open Facility Center, Tokyo Institute of Technology, 2-12-1-N1-10 Ookayama, Meguro-ku, Tokyo 152-8550, Japan
[5] Laboratory for Zero-Carbon Energy, Institute of Innovative Research, Tokyo Institute of Technology, 2-12-1-N1-10 Ookayama, Meguro-ku, Tokyo 152-8550, Japan

[a)] **Author to whom correspondence should be addressed:** yamashita.y.an@m.titech.ac.jp

ABSTRACT

This study proposed a simple method to evaluate the spectral reflectance of the inner wall of a vacuum chamber. A method for calculating spectral emission coefficients by taking the spectral reflectance of the chamber inner wall into account was proposed. Furthermore, plasma diagnosis based on optical emission spectroscopic (OES) measurement was performed so as to obtain radial dependence of electron temperature T_e and density N_e of a radio frequency inductively coupled Argon (Ar) plasma by applying a collisional-radiative model to radially resolved emission spectra of the Ar plasma assuming axial symmetry. In addition, Langmuir probe measurement and electromagnetic simulation were performed and compared with the OES-based plasma diagnosis results. The spectral radiance compensation improved the diagnostic result by 0.6% and 3.1% for T_e and N_e, respectively.

I. INTRODUCTION

Optical emission spectroscopy (OES) has been widely employed in a method of plasma diagnostics as it allows for non-disturbing plasma measurements based on a relatively simple measurement setup. Macroscopic plasma parameters, such as electron temperature T_e and density N_e, are of interest consistently because they govern the reactions in a plasma. The collisional-radiative (CR) model[1] is an atomic–molecular process model that provides the excited-level number density distribution from macroscopic plasma parameters. The excited-level number density distribution of plasmas is experimentally obtained from the spectral emission coefficient, which is defined as the spectral radiant flux emitted per unit solid angle from a unit volume of plasma. Thus, the macroscopic plasma parameters, T_e and N_e, can be obtained by fitting the experimental data with the theoretical value of the excited-level number density distribution determined by the CR model.[2,3] Spatially resolved plasma diagnostics based on OES have been achieved through Abel inversion of multi-position spectral data considering the axial symmetry of the plasma.[4–10] However, the measured spectral radiance includes the sum of both the direct light from the plasma volume and the reflected light at the chamber inner wall.

To calculate the excited-level number density distributions, it has been pointed out in a previous study[11] that the light reflection from the chamber inner walls must be considered. That is, the dependence of optical emission spectra on time was observed during the deposition of thin films in an ICP setup with a two-type wall of different reflectivity. In the highly reflective wall, the dependence of spectra varied periodically due to the thin-film interference on the wall. The diagnostic results of the line-pair method based on the acquired spectra were reported to be significantly different.[11] As for the report that compensates for light reflections on the chamber walls, ray-tracing analysis of visible camera images based on the assumed wall reflectance has been reported in the field of fusion reactor research.[12,13] However, few studies have reported on the spectral properties and influence of the reflected light on chamber inner walls. Moreover, few studies have been conducted on reflectance-aware diagnosis in the field of low-temperature weakly ionized plasmas, particularly semiconductor processing apparatus. An experimental approach to evaluate the light reflection is required to achieve practical diagnostic availability.

The previous reports that corrected for the effect of reflections required bidirectional reflectance distribution function (BRDF) data of the geometrical structures and components in the chamber.

Therefore, although rigorous calculations can be performed, there are practical difficulties, particularly when applying the method to existing plasma devices for the semiconductor industry. This is because measuring the BRDF of each component requires time and effort, such as removing the component and measuring it with a spectrometer.

This study proposed a simple *in situ* method for evaluating the spectral reflectance of the chamber inner wall in this paper. Based on the spectral reflectance calculated using the proposed method, the net spectral emission coefficient of the plasma is obtained. Eventually, T_e and N_e are evaluated based on line spectra fitting.

II. EXPERIMENTAL SETUP OF ICP APPARATUS

Figure 1 shows an inductively coupled plasma (ICP)—generating apparatus employed in this study. The inner wall of the chamber employed anodized aluminum. The chamber inner diameter was Φ = 354 mm. An RF antenna was placed at the top of the chamber over a synthetic quartz window (Φ = 205 mm). The chamber height was 208 mm just below the top window and 193 mm at the outside of the window. The view window (width 110 mm × height 5 mm) of a synthetic quartz (t_{win} = 6 mm thick) was installed on the side wall of the chamber.

III. LIGHT REFLECTION BY CHAMBER INNER WALL

A. Refraction of line-of-sights on the view window

In OES measurement experiments, the directly measurable quantity is the spectral radiance of the air-side surface of the view window. In this study, the line-of-sight is set at an angle to the window surface, which causes a shift in the line-of-sight due to refraction at the window. Figure 2 denotes the concept of the path of the light emitted from the plasma in the chamber to incident on the lens through the view window of the chamber. θ_{air} is defined as the angle between the line-of-sight and the window normal in air. θ_{win} is defined as the angle between the line-of-sight and the window normal in air in the view window. The relationship can be obtained from Snell's law as follows:

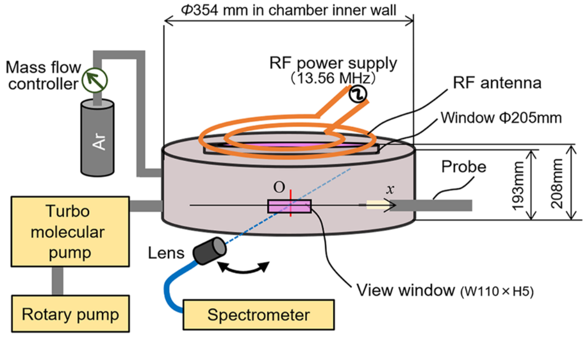

FIG. 1. The schematic diagram of ICP generating apparatus (non-scale). The measured height of the OES and probe are the same, z = 0.

$$\frac{\sin\theta_{\mathrm{air}}}{\sin\theta_{\mathrm{win}}} = \frac{n_{\mathrm{win}}(\lambda)}{n_{\mathrm{air}}(\lambda)}, \tag{1}$$

where λ is the wavelength and $n_{\mathrm{air}}(\lambda)$ and $n_{\mathrm{win}}(\lambda)$ are the spectral refractive index of air and the window, respectively. Therefore, the following relationship is obtained:

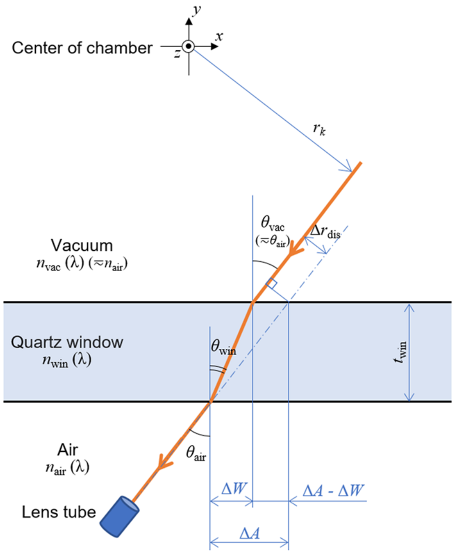

FIG. 2. The conceptual diagram of light propagation in the window. Here, the line-of-sight is parallel to the paper surface and the window interface is vertical to the paper surface.

TABLE I. The angle and nearest radius of line-of-sights of the OES measurement of the plasma.

			Nearest radius for chamber center in vacuum (mm)		
Radius number k	Radius in air (nm)	Incident angle in air $\theta_{\rm win}$ (deg)	Mean r_k (λ = 750.3–978.6 nm)	Min. (λ = 750.3 nm)	Max. (λ = 978.6 nm)
0	0.0	0.000	0.000	0.000	0.000
1	17.7	0.000	17.700	17.700	17.700
2	35.4	0.000	35.400	35.400	35.400
3	53.1	23.893	52.081	52.078	52.083
4	70.8	23.893	69.781	69.778	69.783
5	88.5	23.893	87.481	87.478	87.483
6	106.2	23.893	105.181	105.178	105.183
7	123.9	45.000	121.008	121.003	121.013
8	141.6	45.000	138.708	138.703	138.713
9	159.3	50.894	155.427	155.421	155.433
10	...	...	177.000	...	...

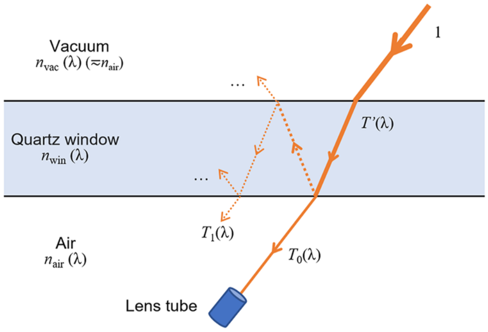

FIG. 3. The spectral radiance observed by the lens is smaller than the spectral radiance emitted by the plasma due to Fresnel reflection.

$$\theta_{\rm win}(\lambda) = \sin^{-1}\left(\frac{n_{\rm air}(\lambda)}{n_{\rm win}(\lambda)}\sin\theta_{\rm air}\right). \tag{2}$$

The spectral refractive index in vacuum $n_{\rm vac}$ is approximately equal to $n_{\rm air}(\lambda)$, $n_{\rm air}(\lambda) \simeq n_{\rm vac}(\lambda) = 1$. Therefore, the incident angle between the line-of-sight and the window normal in vacuum, $\theta_{\rm vac}(\lambda)$, can be assumed to be equal to $\theta_{\rm air}$, $\theta_{\rm air}(\lambda) \simeq \theta_{\rm vac}(\lambda)$. Therefore, $\Delta W(\lambda)$ and $\Delta A(\lambda)$ as shown in Fig. 2 can be obtained as follows:

$$\Delta W(\lambda) = t_{\rm win}\tan\theta_{\rm win}, \tag{3}$$

where $t_{\rm win}$ is the thickness of the view window,

$$\Delta A(\lambda) = t_{\rm win}\tan\theta_{\rm air}. \tag{4}$$

Therefore, the distance between the line-of-sight in the air and the line-of-sight in the vacuum is obtained as follows:

$$\begin{aligned}\Delta r_{\rm dis}(\lambda) &= [\Delta A(\lambda) - \Delta W(\lambda)]\cos\theta_{\rm air}(\lambda)\\ &= t_{\rm win}[\tan\theta_{\rm air}(\lambda) - \tan\theta_{\rm win}(\lambda)]\cos\theta_{\rm air}(\lambda).\end{aligned} \tag{5}$$

On OES measurement of the plasma (Sec. IV B), the positions of the line-of-sights, which were employed in this study, were calculated, as shown in Table I, which were calculated by using the above equations. Note that $n_{\rm win}(\lambda)$ was employed as the literature values[14,15] for the calculation of this study.

Note that in the calculation to obtain radially resolved spectral inversion of this study, r_k is the radius from the center (z axis) of the chamber in the vacuum, which was employed for the calculation of this study ("mean" as shown in Table I) regardless of wavelength because the aberration was sufficiently small to the field of view diameter in the wavelength range, which was employed for the plasma diagnosis in this study.

B. Fresnel on the view window

Due to Fresnel reflection, some of the light emitted from the plasma is reflected at the surface of the window. Figure 3 shows the concept of the Fresnel reflection on the view window. To calculate the spectral emission coefficient of the plasma, the spectral radiance just before the plasma enters the window is required. On the other hand, the quantity that can be directly observed in the experiment is the spectral radiance at the interface between the outside of the window and the air. In this section, we discuss spectral radiance measurements that take these effects into account. (The meanings of the symbols that appear in the following equations are defined, as shown in Fig. 4.) In this section, the relationship $n_{\rm air}(\lambda) = n_{\rm vac}(\lambda) = 1$ is also assumed.

The spectral energy transmittance $T'_{\rm s}(\lambda)$ and the spectral energy reflectance $R'_{\rm s}(\lambda)$ are expressed for the s(TE)-wave on the first incidence from the plasma in vacuum to the vacuum side of the window as follows:[16]

$$T'_{\rm s}(\lambda) = \frac{\sin 2\theta_{\rm air}\,\sin 2\theta_{\rm win}}{\sin^2(\theta_{\rm air}+\theta_{\rm win})}, \tag{6}$$

$$R'_{\rm s}(\lambda) = \frac{\sin^2(\theta_{\rm air}-\theta_{\rm win})}{\sin^2(\theta_{\rm air}+\theta_{\rm win})}. \tag{7}$$

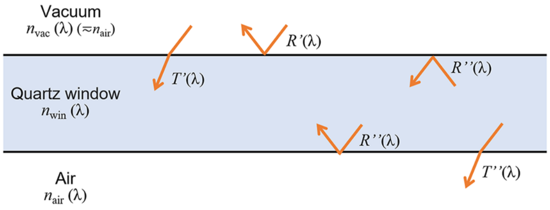

FIG. 4. Meaning of the symbols for transmittance and reflectance.

Similarly, the spectral energy transmittance $T'_p(\lambda)$ and the spectral energy reflectance $R'_p(\lambda)$ are expressed for the p(TM)-wave as follows:[16]

$$T'_p(\lambda) = \frac{\sin 2\theta_{air}\ \sin 2\theta_{win}}{\sin^2(\theta_{air} + \theta_{win})\ \cos^2(\theta_{air} - \theta_{win})}, \tag{8}$$

$$R'_p(\lambda) = \frac{\tan^2(\theta_{air} - \theta_{win})}{\tan^2(\theta_{air} + \theta_{win})}. \tag{9}$$

From Eqs. (6) and (7), the spectral energy transmittance from the window to the air on the window—the air boundary, $T''_s(\lambda)$, and the spectral energy reflectance from the window to the window on the window—the air or vacuum boundary, $R''_s(\lambda)$, are expressed as follows:

$$T''_s(\lambda) = T'_s(\lambda), \tag{10}$$

$$R''_s(\lambda) = R'_s(\lambda). \tag{11}$$

From Eqs. (8) and (9), the spectral energy transmittance $T''_p(\lambda)$ and the spectral energy reflectance $R''_p(\lambda)$ are expressed for the p-wave as follows:

$$T''_p(\lambda) = T'_p(\lambda), \tag{12}$$

$$R''_p(\lambda) = R'_p(\lambda). \tag{13}$$

The spectral transmittance of the zeroth-order transmitted light, that is, the ratio of the incident light power on the vacuum–window interface to the power of the light passing through the vacuum–window interface and further right away passing through the window–vacuum interface (as shown in Fig. 3), is given for s and p waves as follows, respectively:

$$T_{s0}(\lambda) = T'_s(\lambda)\ T''_s(\lambda), \tag{14}$$

$$T_{p0}(\lambda) = T'_p(\lambda)\ T''_p(\lambda). \tag{15}$$

Therefore, the spectral transmittance of the zeroth-order transmitted light is given for the natural polarization wave as follows:

$$T_0(\lambda) = \frac{1}{2}[T_{s0}(\lambda) + T_{p0}(\lambda)]. \tag{16}$$

Figure 5 denotes the calculation result of Eq. (16) for the experimental setup of this study.

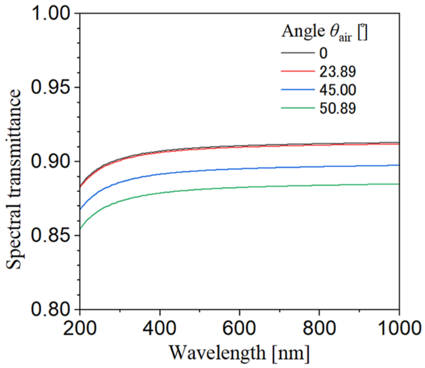

FIG. 5. The calculation result of spectral transmittance $T_0(\lambda)$ of the zeroth-order transmitted light on the 6 mm thick quartz window. The spectral transmittance is expressed as the power ratio to incident light.

Note that the spectral transmittance of the first-order transmitted light, that is, the light passing through the vacuum–window interface, reflected on the window side of the window–air boundary, reflected on the window side of the window–vacuum boundary, and transmitted on the window–air boundary, is given for s and p-waves as follows, respectively:

$$T_{s1}(\lambda) = T'_s(\lambda)\ \{R''_s(\lambda)\}^2\ T''_s(\lambda), \tag{17}$$

$$T_{p1}(\lambda) = T'_p(\lambda)\ \{R''_s(\lambda)\}^2\ T''_p(\lambda). \tag{18}$$

For natural polarization light, the transmittance is expressed as follows:

$$T_1(\lambda) = \frac{1}{2}[T_{s1}(\lambda) + T_{p1}(\lambda)]. \tag{19}$$

The calculation result of $T_1(\lambda)$ for the experimental setup of this study is shown in Fig. 6.

In this study, only the zeroth-order transmitted light was assumed to enter the lens. This is because the higher-order transmitted light above the first order has less energy than zero-order

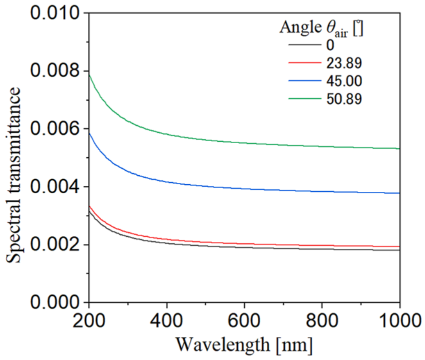

FIG. 6. The calculation result of spectral transmittance $T_1(\lambda)$ of first-order transmitted light on the 6 mm thick quartz window. The spectral transmittance is expressed as the power ratio to incident light.

transmitted light (as shown in Fig. 6) and higher-order transmitted light above the second order has even lower intensity. Moreover, the first-order or higher-order transmitted light is incident at a displaced position except at vertical incidence. In addition, the window is sufficiently thick relative to the wavelength that thin-film interference phenomena are unlikely to be involved.

Therefore, the spectral radiance on the vacuum side surface of the window is calculated as follows:

$$L_{\mathrm{I}}(\lambda) = \frac{L'_{\mathrm{I}}(\lambda)}{T_0(\lambda)}, \tag{20}$$

where $L'_{\mathrm{I}}(\lambda)$ is the spectral radiance on the air side surface of the window, which was experimentally obtained by the OES measurement experiment.

C. Evaluation of spectral reflectance of inner wall

This section discusses the strategy of obtaining the average spectral reflectance of the chamber inner wall. In this study, the chamber was regarded as an integrating sphere on the inner wall to facilitate a simplified evaluation to measure the spectral reflectance of the chamber. However, an integrating sphere is generally spherical, and its inner surface is composed of a diffuse reflective material according to the cosine law, and the area of the aperture port is designed to be sufficiently small to the area of the diffuse reflective material. In contrast, the shape of this chamber is cylindrical. The inner surface of the chamber consists of anodized aluminum (no coloring; the thickness of the anodic oxide film was ~6–10 μm; the fine hole was sealed by using the nickel acetate method), which does not guarantee compliance with the cosine law. Furthermore, the chamber has windows, a gas inlet, and exhaust ports. Therefore, strictly speaking, this chamber cannot be regarded as an integrating sphere, and differences will arise, but for the sake of simplicity in optical modeling, such an assumption was made.

In this study, the following method for measuring the average spectral reflectance of the chamber inner wall was applied. Note that this method is similar to the method used to evaluate the average spectral reflectance of the inner wall of the integrating sphere.[17] (1) A graphite plate that has surface area S_{b} was employed as the reference reflector. The spectral total reflectance $R_{\mathrm{b}}(\lambda)$ of the graphene reference reflector was calibrated with a UV–VIS–NIR spectrophotometer (U-4100, Hitachi High-Tech Science) beforehand. Note that the spectral total reflectance is the sum of the specular and diffuse reflected spectral radiant flux relative to the sum of the incident spectral radiant flux. (2) Figure 7 illustrates the conceptual setup of the spectral-reflectance measurement. An incandescent lamp (G-1282H, Asahi Electric) was placed inside the chamber. To prevent direct light from the lamp from entering directly the reference graphene reflector and lens, the lamp was covered with a douser. The lamp works the same as a self-absorption measurement lamp in a spherical light fluxmeter. In other words, the reference reflector or the lens is indirectly illuminated by multiple reflected lights on the chamber inner wall. Furthermore, a lens tube with a diffuse transmission plate was set on the quartz view window of the chamber side wall to measure spectral-count value, which is proportional to spectral irradiance at the inner wall surface. The lens tube was connected to the spectrometer (MS3504i, SOL instruments) with the charge coupled device (CCD) detector (DU420A-OE, Andor Technology). (3) The spectral-count value $I_{\mathrm{g}}(\lambda)$ was measured without the reference reflector in the chamber [as shown in (b) of Fig. 7]. (4) The reference reflector was placed on the chamber inner wall, as shown in (a) of Fig. 7. The spectral-count value $I_{\mathrm{c}}(\lambda)$ was measured with the reference reflector in the chamber.

The derivation of the spectral reflectance of the chamber wall is as follows. The spectral irradiance at the inner wall surface without and with the reference reflector in the chamber, $E_{\mathrm{g}}(\lambda)$ and $E_{\mathrm{c}}(\lambda)$, is as follows, respectively:

$$\begin{aligned} E_{\mathrm{g}}(\lambda) &= K_1(\lambda)\, I_{\mathrm{g}}(\lambda), \\ E_{\mathrm{c}}(\lambda) &= K_1(\lambda)\, I_{\mathrm{c}}(\lambda), \end{aligned} \tag{21}$$

where $K_1(\lambda)$ is a constant, which is determined by the system's spectral response. The spectral irradiance at the inner wall surface $E_{\mathrm{g}}(\lambda)$ is calculated as follows:[17]

$$E_{\mathrm{g}}(\lambda) = K_2(\lambda)\frac{R_{\mathrm{g}}(\lambda)}{1 - R_{\mathrm{g}}(\lambda)}, \tag{22}$$

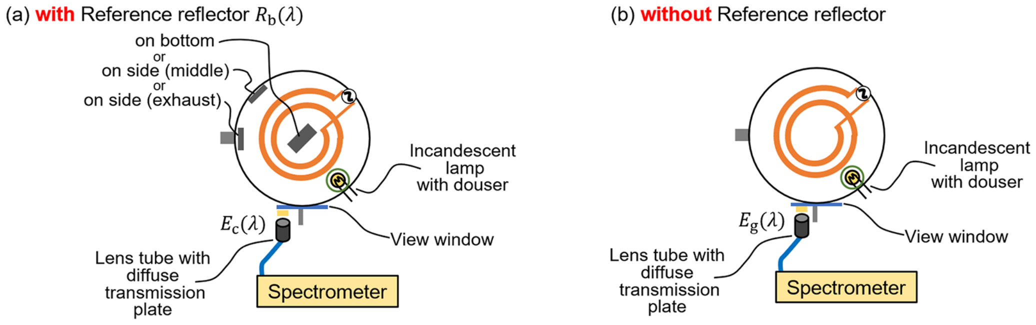

FIG. 7. The top view diagram of spectral-reflectance measurement. In (a), a reference reflector was placed at one of the locations. To investigate how well the chamber acts as an integrating sphere, the dependence of the spectral reflectance of the chamber inner wall on the position of the reference reflector was measured. In (b), the reference reflector was not placed.

where $K_2(\lambda)$ is a constant, which is determined by the total spectral radiant flux of the incandescent lamp and the chamber inner size, and $R_g(\lambda)$ is the spectral reflectance of the inner wall. When the reference reflector is installed in the chamber, the average spectral reflectance is expressed as follows:

$$\begin{aligned} R_c(\lambda) &= \frac{S_g - S_b}{S_g} R_g(\lambda) + \frac{S_b}{S_g} R_b(\lambda) \\ &= (1-\alpha) R_g(\lambda) + \alpha R_b(\lambda), \end{aligned} \tag{23}$$

where S_g is the surface area of the chamber inner wall, $\alpha = S_b/S_g$ $(0 < \alpha < 1)$. The spectral irradiance at the inner wall surface with the reference reflector is as follows:

$$E_c(\lambda) = K_2(\lambda) \frac{R_c(\lambda)}{1 - R_c(\lambda)}. \tag{24}$$

When $F(\lambda) = E_c(\lambda)/E_g(\lambda)$ is defined, the following relationship is obtained:

$$\begin{aligned} F(\lambda) &= \frac{E_c(\lambda)}{E_g(\lambda)} \\ &= \frac{R_c(\lambda)}{1 - R_c(\lambda)} \frac{1 - R_g(\lambda)}{R_g(\lambda)} \quad (0 < F(\lambda) < 1), \end{aligned} \tag{25}$$

and from Eq. (21), we have

$$F(\lambda) = \frac{I_c(\lambda)}{I_g(\lambda)}. \tag{26}$$

The following equation is obtained using Eqs. (23) and (25) and eliminating $R_c(\lambda)$:

$$A R_g^2(\lambda) + B R_g(\lambda) + C = 0, \tag{27}$$

where

$$\begin{cases} A = (1-\alpha)[1 - F(\lambda)] \ > 0, \\ B = [1 - \alpha R_b(\lambda)][F(\lambda) - 1] + \alpha \ > 0, \\ C = -\alpha R_b(\lambda) \ < 0. \end{cases} \tag{28}$$

$R_g(\lambda)$ must be $0 < R_g(\lambda) < 1$. Therefore, $R_g(\lambda)$ is obtained as follows:

$$R_g(\lambda) = \frac{-B + \sqrt{B^2 - 4AC}}{2A}. \tag{29}$$

Therefore, $R_g(\lambda)$ was obtained and based on Eqs. (26) and (29) from the experimental values $I_g(\lambda)$ and $I_c(\lambda)$.

D. Calculation of net spectral emission coefficient of plasma

In this section, we discuss the strategy for obtaining the radial distribution of the spectral emission coefficients of the plasma from the OES measurement of plasmas. In this study, the spatial distribution of the spectral emission coefficient of the plasma was assumed to be z axis cylindrical symmetry. Let $\varepsilon(\lambda, r)$ be the spectral emission coefficient of the microvolume element $d\boldsymbol{v}$ at radius r on the x–y plane and z on the z axis; the total spectral emission flux from $d\boldsymbol{v}$, $d\Phi_T(\lambda, r)$, is expressed as follows:

$$d\Phi_T(\lambda, r) = 4\pi\, \varepsilon(\lambda, r)\, d\boldsymbol{v}. \tag{30}$$

Therefore, the spectral total radiation flux of the plasma in the chamber, $\Phi_T(\lambda)$, is expressed as follows:

$$\begin{aligned} \Phi_T(\lambda) &= \int_{\boldsymbol{v}} d\Phi_T(\lambda, r) \\ &= \int_{\boldsymbol{v}} 4\pi\, \varepsilon(\lambda, r)\, d\boldsymbol{v}. \end{aligned} \tag{31}$$

Applying the variable transformation from the rectangular coordinate system to the cylindrical coordinate system $(x, y, z) \to (r, \theta, z)$, the following equation can be obtained because $d\boldsymbol{v} = r\, dr\, d\theta\, dz$:

$$\begin{aligned} \Phi_T(\lambda) &= \int_{z''}^{z'} \int_0^{2\pi} \int_0^R 4\pi\, \varepsilon(\lambda, r)\, r\, dr\, d\theta\, dz \\ &= 8\pi^2 H \int_0^R \varepsilon(\lambda, r)\, r\, dr, \end{aligned} \tag{32}$$

where R is the cylinder inner radius of the chamber, z' and z'' are the upper and lower position of the chamber along the z axis, respectively, and $H = z' - z''$ is the height along the z axis of the chamber.

The spectral irradiance by the multiple reflections illuminating the inner wall surface has position dependence. Therefore, as mentioned in the Introduction, to rigorously calculate the effect of multiple reflections by the inner wall, it is necessary to perform calculations using the ray-tracing method. The method requires the geometry of the inner wall and BRDF, which is a complex calculation. However, in this study, we propose a calculation method by "average" spectral irradiance for multiple reflections on the chamber inner wall surface. We were inspired by the "luminous flux method" used in the field of lighting engineering to develop the proposed method. The proposed method is undeniable that the calculation error increases compared to the ray-tracing method. However, the proposed method is computationally simpler than the ray-tracing method. Furthermore, the proposed method is especially useful for multiple reflection correction in situations where it is not possible to measure the BRDF of all the components of the inner wall, for example, in existing plasma devices. The proposed methodology is as follows.

The average spectral irradiance on the chamber inner wall by the multiple reflected light of $\Phi_T(\lambda)$ is as follows:[17]

$$E_{refl}(\lambda) = \frac{R_g(\lambda)\, \Phi_T(\lambda)}{[1 - R_g(\lambda)]\, S_g}. \tag{33}$$

Assuming Lambertian reflection, the spectral radiance on the chamber inner wall by the multiple reflected light of $\Phi_T(\lambda)$ is expressed as follows:

$$\begin{aligned} L_{refl}(\lambda) &= \frac{R_g(\lambda)}{\pi} E_{refl}(\lambda) \\ &= \frac{R_g^2(\lambda)\, \Phi_T(\lambda)}{\pi [1 - R_g(\lambda)]\, S_g}. \end{aligned} \tag{34}$$

Inserting Eq. (32), we get

$$L_{\text{refl}}(\lambda) = \frac{R_g^2(\lambda)}{\pi[1 - R_g(\lambda)]\, S_g}\, 8\pi^2 H \int_0^R \varepsilon(\lambda, r)\, r\, \mathrm{d}r. \tag{35}$$

The spectral radiance on the window vacuum side surface of the line-of-sight whose nearest distance to origin $x = x''$ on the x–y plane, $L_{\mathrm{I}}(\lambda, x'', z)$, is the sum of the spectral radiance due to direct light from the plasma in the line-of-sight and the multiple reflections of light emitted from the entire plasma,

$$L_{\mathrm{I}}(\lambda, x'', z) = L_{\mathrm{D}}(\lambda, x'', z) + L_{\text{refl}}(\lambda), \tag{36}$$

where $L_{\mathrm{D}}(\lambda, x'', z)$ is the spectral radiance at the window surface on $x = x''$ due to direct light caused by the micro-volume elements of the plasma on the line-of-sight, which through on the x–y plane and whose nearest point to the origin in the line-of-sight is $(x, y, z) = (x'', 0, 0)$ as follows:

$$L_{\mathrm{D}}(\lambda, x'', z) = \int_{-\sqrt{R2-x''2}}^{\sqrt{R^2-x''2}} \varepsilon(\lambda, x'', y, z)\, \mathrm{d}y. \tag{37}$$

As $\varepsilon(\lambda, x'', y, z)$ is the even function of y, the following relationship can be obtained:

$$L_{\mathrm{D}}(\lambda, x'', z) = \int_0^{\sqrt{R2-x''2}} 2\,\varepsilon(\lambda, x'', y, z)\, \mathrm{d}y. \tag{38}$$

By the variable transformation from the rectangular coordinate system to the cylindrical coordinate system, $(x, y, z) \to (r, \theta, z)$, we get the following relationship as $x''^2 + y^2 = r^2$ and $\mathrm{d}y = r\,\mathrm{d}r/\sqrt{r^2 - x''^2}$. Furthermore, assuming z axis symmetry in the x–y plane, we can get $r'' = x''$. Therefore, Eq. (38) can be expressed as follows:

$$\begin{aligned} L_{\mathrm{D}}(\lambda, r'', z) &= L_{\mathrm{D}}(\lambda, x'', z) \\ &= \int_{r''}^{R} 2\,\varepsilon(\lambda, r, z)\, \frac{r}{\sqrt{r^2 - r''^2}} \mathrm{d}r. \end{aligned} \tag{39}$$

From now, the chamber inner diameter R is divided into n segments, and r_k $(k = 0, 1, \ldots, n-1)$ is defined as the kth radius. Note that $r_0 = 0$ and $r_n = R$ are the center and the inner wall of the chamber, respectively. Therefore, Eq. (39) can be expressed as follows:

$$\begin{aligned} L_{\mathrm{D}}(\lambda, r_k, z) &= \int_{r_k}^{R} 2\,\varepsilon(\lambda, r, z)\, \frac{r}{\sqrt{r^2 - r_k^2}}\, \mathrm{d}r \\ &= \int_{r_k}^{r_{k+1}} 2\,\varepsilon(\lambda, r, z)\, \frac{r}{\sqrt{r^2 - r_k^2}}\, \mathrm{d}r + \int_{r_{k+1}}^{r_{k+2}} 2\,\varepsilon(\lambda, r, z)\, \frac{r}{\sqrt{r^2 - r_k^2}}\, \mathrm{d}r + \cdots + \int_{r_{n-1}}^{R} 2\,\varepsilon(\lambda, r, z)\, \frac{r}{\sqrt{r^2 - r_k^2}}\, \mathrm{d}r \\ &= \sum_{k'=k}^{n-1} \int_{r_k}^{r_{k+1}} 2\,\varepsilon(\lambda, r, z)\, \frac{r}{\sqrt{r^2 - r_k^2}}\, \mathrm{d}r. \end{aligned} \tag{40}$$

Furthermore, $\varepsilon(\lambda, r, z)$ is assumed to be the first-order polynomial on the assumption of uniformity in the z axis direction, as in the following equation and in Fig. 8:

$$\varepsilon(\lambda, r) = \begin{cases} a_k(\lambda) + b_k(\lambda)\, r, & \text{where} \quad r_k \le r < r_{k+1} \quad \text{and} \quad k = 0, 1, \ldots, n-2 \\ (\text{for } 0 \le r < r_{n-1}), & \\ a_{n-2}(\lambda) + b_{n-2}(\lambda)\, r_{n-1} & (\text{for } r_{n-1} \le r < R). \end{cases} \tag{41}$$

Equation (41) can be expressed for $0 \le r < r_{n-1}$ as follows:

$$\begin{aligned} a_k(\lambda) + b_k(\lambda)\, r_{k+1} &= a_{k+1}(\lambda) + b_{k+1}(\lambda)\, r_{k+1}, \\ \Leftrightarrow a_{k+1}(\lambda) &= a_k(\lambda) + [b_k(\lambda) - b_{k+1}(\lambda)] r_{k+1}, \\ \therefore a_k(\lambda) &= a_0(\lambda) + \sum_{k'=0}^{k-1} [b_{k'}(\lambda) - b_{k'+1}(\lambda)] r_{k'+1}. \end{aligned} \tag{42}$$

Therefore, Eq. (41) can be expressed as follows:

$$\varepsilon(\lambda, r) = \begin{cases} a_0(\lambda) + b_k(\lambda)\, r + \displaystyle\sum_{k'=0}^{k-1} [b_{k'}(\lambda) - b_{k'+1}(\lambda)] r_{k'+1}, & \text{where} \quad r_k \le r < r_{k+1} \quad \text{and} \quad k = 0, 1, \ldots, n-2 \quad (\text{for } 0 \le r < r_{n-1}), \\ a_0(\lambda) + b_{n-2}(\lambda)\, r_{n-1} + \displaystyle\sum_{k'=0}^{n-3} [b_{k'}(\lambda) - b_{k'+1}(\lambda)] r_{k'+1} & (\text{for } r_{n-1} \le r < R). \end{cases} \tag{43}$$

Inserting Eq. (43) into Eq. (40), we get

$$
\begin{aligned}
L_{\mathrm{D}}(\lambda,\, r_k) &= \sum_{k'=k}^{n-1} \int_{r_k}^{r_{k+1}} 2\,\varepsilon(\lambda,\, r)\, \frac{r}{\sqrt{r^2 - r_k^2}}\, \mathrm{d}r = \sum_{k'=k}^{n-2} \left[\int_{r_{k'}}^{r_{k'+1}} 2\,\varepsilon(\lambda,\, r)\, \frac{r}{\sqrt{r^2 - r_k^2}}\, \mathrm{d}r \right] + \int_{r_{n-1}}^{r_n = R} 2\,\varepsilon(\lambda,\, r)\, \frac{r}{\sqrt{r^2 - r_k^2}}\, \mathrm{d}r \\
&= \sum_{k'=k}^{n-2} \left\{ \int_{r_{k'}}^{r_{k'+1}} 2\left[a_{k'}(\lambda) + b_{k'}(\lambda)\, r\right] \frac{r}{\sqrt{r^2 - r_k^2}}\, \mathrm{d}r \right\} + \int_{r_{n-1}}^{r_n = R} 2\left[a_{n-2}(\lambda) + b_{n-2}(\lambda)\, r_{n-1}\right] \frac{r}{\sqrt{r^2 - r_k^2}}\, \mathrm{d}r \\
&= 2\sum_{k'=k}^{n-2} \left\{ \int_{r_{k'}}^{r_{k'+1}} a_{k'}(\lambda)\, \frac{r}{\sqrt{r^2 - r_k^2}}\, \mathrm{d}r + \int_{r_{k'}}^{r_{k'+1}} b_{k'}(\lambda)\, \frac{r^2}{\sqrt{r^2 - r_k^2}}\, \mathrm{d}r \right\} + 2\int_{r_{n-1}}^{r_n = R} \left[a_{n-2}(\lambda) + b_{n-2}(\lambda)\, r_{n-1}\right] \frac{r}{\sqrt{r^2 - r_k^2}}\, \mathrm{d}r \\
&= 2\sum_{k'=k}^{n-2} \left[a_{k'}(\lambda)\sqrt{r^2 - r_k^2} + b_{k'}(\lambda)\left\{ \frac{r\sqrt{r^2 - r_k^2}}{4} + \frac{r_k^2}{4} \ln\left| r + \sqrt{r^2 - r_k^2} \right| \right\} \right]_{r_{k'}}^{r_{k'+1}} + 2\left\{a_{n-2}(\lambda) + b_{n-2}(\lambda)\, r_{n-1}\right\} \left[\sqrt{r^2 - r_k^2} \right]_{r_{n-1}}^{r_n = R} \\
&= 2\sum_{k'=k}^{n-2} a_{k'}(\lambda) \left[\sqrt{r_{k'+1}^2 - r_k^2} - \sqrt{r_{k'}^2 - r_k^2} \right] + 2\sum_{k'=k}^{n-2} b_{k'}(\lambda) \left\{ \frac{r_{k'+1}\sqrt{r_{k'+1}^2 - r_k^2} - r_{k'}\sqrt{r_{k'}^2 - r_k^2}}{4} + \frac{r_k^2}{4} \ln\left| \frac{r_{k'+1} + \sqrt{r_{k'+1}^2 - r_k^2}}{r_{k'} + \sqrt{r_{k'}^2 - r_k^2}} \right| \right\} \\
&\quad + 2\left\{a_{n-2}(\lambda) + b_{n-2}(\lambda)\, r_{n-1}\right\} \left[\sqrt{r_n^2 - r_k^2} - \sqrt{r_{n-1}^2 - r_k^2} \right] \\
&= 2\sum_{k'=k}^{n-2} \left[a_0(\lambda) + \sum_{k''=0}^{k'-1} \left[b_{k''}(\lambda) - b_{k''+1}(\lambda)\right] r_{k'+1} \right] \left[\sqrt{r_{k'+1}^2 - r_k^2} - \sqrt{r_{k'}^2 - r_k^2} \right] \\
&\quad + 2\sum_{k'=k}^{n-2} b_{k'}(\lambda) \left\{ \frac{r_{k'+1}\sqrt{r_{k'+1}^2 - r_k^2} - r_{k'}\sqrt{r_{k'}^2 - r_k^2}}{4} + \frac{r_k^2}{4} \ln\left| \frac{r_{k'+1} + \sqrt{r_{k'+1}^2 - r_k^2}}{r_{k'} + \sqrt{r_{k'}^2 - r_k^2}} \right| \right\} \\
&\quad + 2\left\{ \left[a_0(\lambda) + \sum_{k'=0}^{n-3} \left[b_{k'}(\lambda) - b_{k'+1}(\lambda)\right] r_{k'+1} \right] + b_{n-2}(\lambda)\, r_{n-1} \right\} \left[\sqrt{r_n^2 - r_k^2} - \sqrt{r_{n-1}^2 - r_k^2} \right] \\
&= 2\sum_{k'=k}^{n-2} \left[a_0(\lambda) + \sum_{k''=0}^{k'-1} \left[b_{k''}(\lambda) - b_{k''+1}(\lambda)\right] r_{k'+1} \right] C_1(k', k) \\
&\quad + 2\sum_{k'=k}^{n-2} b_{k'}(\lambda) C_2(k', k) + 2\left\{ \left[a_0(\lambda) + \sum_{k'=0}^{n-3} \left[b_{k'}(\lambda) - b_{k'+1}(\lambda)\right] r_{k'+1} \right] + b_{n-2}(\lambda)\, r_{n-1} \right\} C_3(n, k) \\
&= 2\sum_{k'=k}^{n-2} a_0(\lambda)\, C_1(k', k) + \left[2\sum_{k'=k}^{n-2} \sum_{k''=0}^{k'-1} \left[b_{k''}(\lambda) - b_{k''+1}(\lambda)\right] r_{k'+1}\, C_1(k', k) \right] \\
&\quad + 2\sum_{k'=k}^{n-2} b_{k'}(\lambda) C_2(k', k) + 2C_3(n, k)\, a_0(\lambda) + \left\{ 2C_3(n, k) \sum_{k'=0}^{n-3} \left[b_{k'}(\lambda) - b_{k'+1}(\lambda)\right] r_{k'+1} \right\} + 2b_{n-2}(\lambda)\, r_{n-1} C_3(n, k) \\
&= 2\sum_{k'=k}^{n-2} a_0(\lambda)\, C_1(k', k) + \left[2\sum_{k'=k}^{n-2} \sum_{k''=0}^{k'-1} b_{k''}(\lambda) r_{k'+1}\, C_1(k', k) - 2\sum_{k'=k}^{n-2} \sum_{k''=1}^{k'} b_{k''}(\lambda) r_{k'+1}\, C_1(k', k) \right] \\
&\quad + 2\sum_{k'=k}^{n-2} b_{k'}(\lambda) C_2(k', k) + 2C_3(n, k)\, a_0(\lambda) + \left\{ 2C_3(n, k) \sum_{k'=0}^{n-3} b_{k'}(\lambda) r_{k'+1} - 2C_3(n, k) \sum_{k'=1}^{n-2} b_{k'}(\lambda) r_{k'+2} \right\} + 2b_{n-2}(\lambda)\, r_{n-1} C_3(n, k),
\end{aligned}
\tag{44}
$$

where C_1, C_2, C_3 are as follows, respectively,

$$
\begin{aligned}
C_1(k', k) &= \left[\sqrt{r_{k'+1}^2 - r_k^2} - \sqrt{r_{k'}^2 - r_k^2} \right], \\
C_2(k', k) &= \left\{ \frac{r_{k'+1}\sqrt{r_{k'+1}^2 - r_k^2} - r_{k'}\sqrt{r_{k'}^2 - r_k^2}}{4} + \frac{r_k^2}{4} \ln\left| \frac{r_{k'+1} + \sqrt{r_{k'+1}^2 - r_k^2}}{r_{k'} + \sqrt{r_{k'}^2 - r_k^2}} \right| \right\}, \\
C_3(n, k) &= \left[\sqrt{r_n^2 - r_k^2} - \sqrt{r_{n-1}^2 - r_k^2} \right].
\end{aligned}
$$

Similarly, applying Eq. (43) to Eq. (35), we obtain

$$
\begin{aligned}
L_{\mathrm{refl}}(\lambda) &= \frac{R_{\mathrm{g}}^2(\lambda)}{\pi[1-R_{\mathrm{g}}(\lambda)]\,S_{\mathrm{g}}}\,8\pi^2 H\left[\int_{r_0}^{r_1}\varepsilon(\lambda,r)\,r\,\mathrm{d}r+\int_{r_1}^{r_2}\varepsilon(\lambda,r)\,r\,\mathrm{d}r+\cdots+\int_{r_{n-1}}^{R}\varepsilon(\lambda,r)\,r\,\mathrm{d}r\right]\\
&= \frac{R_{\mathrm{g}}^2(\lambda)}{\pi[1-R_{\mathrm{g}}(\lambda)]\,S_{\mathrm{g}}}\,8\pi^2 H\sum_{k'=0}^{n-1}\int_{r_{k'}}^{r_{k'+1}}\varepsilon(\lambda,r)\,r\,\mathrm{d}r\\
&= \frac{R_{\mathrm{g}}^2(\lambda)}{\pi[1-R_{\mathrm{g}}(\lambda)]\,S_{\mathrm{g}}}\,8\pi^2 H\left[\sum_{k'=0}^{n-2}\int_{r_{k'}}^{r_{k'+1}}\varepsilon(\lambda,r)\,r\,\mathrm{d}r+\int_{r_{n-1}}^{r_n}\varepsilon(\lambda,r)\,r\,\mathrm{d}r\right]\\
&= \frac{R_{\mathrm{g}}^2(\lambda)}{\pi[1-R_{\mathrm{g}}(\lambda)]\,S_{\mathrm{g}}}\,8\pi^2 H\left\{\sum_{k'=0}^{n-2}\left[\int_{r_{k'}}^{r_{k'+1}}[a_{k'}(\lambda)\,r+b_{k'}(\lambda)\,r^2]\,\mathrm{d}r\right]+\int_{r_{n-1}}^{r_n}[a_{n-2}(\lambda)+b_{n-2}(\lambda)\,r_{n-1}]\,r\,\mathrm{d}r\right\}\\
&= \frac{R_{\mathrm{g}}^2(\lambda)}{\pi[1-R_{\mathrm{g}}(\lambda)]\,S_{\mathrm{g}}}\,8\pi^2 H\left\{\sum_{k'=0}^{n-2}\left[a_{k'}(\lambda)\frac{r^2}{2}+b_{k'}(\lambda)\frac{r^3}{3}\right]_{r_{k'}}^{r_{k'+1}}+\{a_{n-2}(\lambda)+b_{n-2}(\lambda)\,r_{n-1}\}\left[\frac{r^2}{2}\right]_{r_{n-1}}^{r_n}\right\}\\
&= \frac{R_{\mathrm{g}}^2(\lambda)}{\pi[1-R_{\mathrm{g}}(\lambda)]\,S_{\mathrm{g}}}\,8\pi^2 H\left\{\sum_{k'=0}^{n-2}\left[a_{k'}(\lambda)\frac{r_{k'+1}^2-r_{k'}^2}{2}+b_{k'}(\lambda)\frac{r_{k'+1}^3-k_{k'}^3}{3}\right]+\{a_{n-2}(\lambda)+b_{n-2}(\lambda)\,r_{n-1}\}\frac{r_n^2-r_{n-1}^2}{2}\right\}\\
&= \frac{R_{\mathrm{g}}^2(\lambda)}{\pi[1-R_{\mathrm{g}}(\lambda)]\,S_{\mathrm{g}}}\,8\pi^2 H\left\{\left[\sum_{k'=0}^{n-2}a_{k'}(\lambda)\frac{r_{k'+1}^2-r_{k'}^2}{2}+\sum_{k'=0}^{n-2}b_{k'}(\lambda)\frac{r_{k'+1}^3-k_{k'}^3}{3}\right]+[a_{n-2}(\lambda)+b_{n-2}(\lambda)\,r_{n-1}]\frac{r_n^2-r_{n-1}^2}{2}\right\}\\
&= \frac{R_{\mathrm{g}}^2(\lambda)}{\pi[1-R_{\mathrm{g}}(\lambda)]\,S_{\mathrm{g}}}\,8\pi^2 H\cdot\left\{\sum_{k'=0}^{n-2}\left[a_0(\lambda)+\sum_{k''=0}^{k'-1}[b_{k''}(\lambda)-b_{k''+1}(\lambda)]r_{k''+1}\right]C_4(k')\right.\\
&\quad\left.+\sum_{k'=0}^{n-2}b_{k'}(\lambda)\,C_5(k')+\left[a_0(\lambda)+\sum_{k'=0}^{n-3}[b_{k'}(\lambda)-b_{k'+1}(\lambda)]r_{k'+1}+b_{n-2}(\lambda)\,r_{n-1}\right]C_4(n-1)\right\}
\end{aligned}
\tag{45}
$$

where $C_4(k')=\dfrac{r_{k'+1}^2-r_{k'}^2}{2}$, $C_5(k')=\dfrac{r_{k'+1}^3-k_{k'}^3}{3}$

$$
\begin{aligned}
&= \frac{R_{\mathrm{g}}^2(\lambda)}{\pi[1-R_{\mathrm{g}}(\lambda)]\,S_{\mathrm{g}}}\,8\pi^2 H\cdot\left[\sum_{k'=0}^{n-2}a_0(\lambda)C_4(k')+\sum_{k'=0}^{n-2}\sum_{k''=0}^{k'-1}b_{k''}(\lambda)r_{k''+1}C_4(k')-\sum_{k'=0}^{n-2}\sum_{k''=1}^{k'}b_{k''}(\lambda)r_{k''}\,C_4(k')\right.\\
&\quad\left.+\sum_{k'=0}^{n-2}b_{k'}(\lambda)\,C_5(k')+a_0(\lambda)\,C_4(n-1)+\sum_{k'=0}^{n-3}b_{k'}(\lambda)\,r_{k'+1}\,C_4(n-1)-\sum_{k'=1}^{n-2}b_{k'}(\lambda)r_{k'}\,C_4(n-1)+b_{n-2}(\lambda)\,r_{n-1}\,C_4(n-1)\right].
\end{aligned}
$$

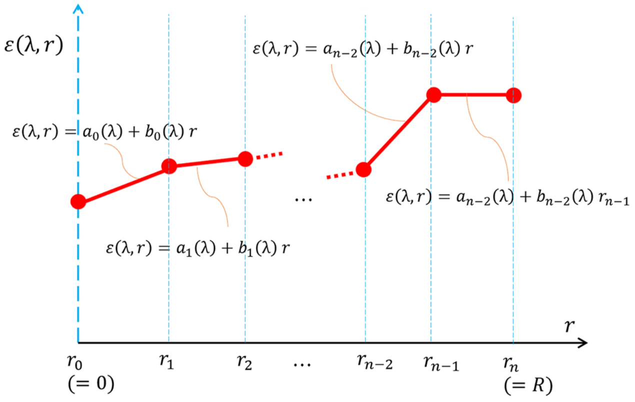

FIG. 8. The conceptual diagram of Eq. (41).

Assuming that the z axis direction is independent, Eq. (36) can be expressed as follows:

$$L_{\mathrm{I}}(\lambda,r_k)=L_{\mathrm{D}}(\lambda,r_k)+L_{\mathrm{refl}}(\lambda). \tag{46}$$

Therefore, $L_{\mathrm{I}}(\lambda,r_k)$ can be expressed as the function of $a_0(\lambda)$ and $b_k(\lambda)$, where $L_{\mathrm{I}}(\lambda,r_k)$ is the kth line-of-sight of the spectral radiance on the vacuum side surface of the window, which is equal to $L_I(\lambda)$ of Eq. (20).

In this study, $a_0(\lambda)$ and $b_k(\lambda)$ were obtained based on the numerical fitting of the calculated and experimental of $L_{\mathrm{I}}(\lambda,r_k)$. Furthermore, $\varepsilon(\lambda,r_k)$ were calculated from the obtained $a_0(\lambda)$ and $b_k(\lambda)$.

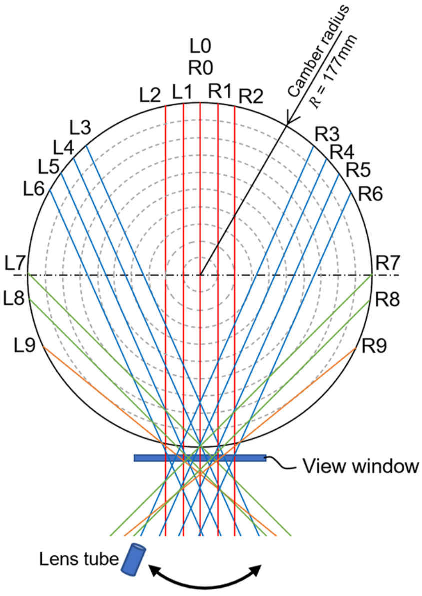

FIG. 9. The schematic diagram of the line of sight of OES measurement. Here, "L *l*" and "R *l*" denote the *l*th lines of sight on left and right sides, respectively. Note that the line of sight placement was set the same as in Ref. 18.

IV. PLASMA DIAGNOSIS

A. Experimental condition of plasma diagnosis

Figure 1 shows that Argon (Ar) gas of 10 SCCM was supplied into the chamber via a mass flow controller. Furthermore, the chamber was evacuated using turbomolecular and rotary pumps. The base pressure of the vacuum chamber was 1.6×10^{-3} Pa. The 13.56 MHz RF power of 300 W was applied to the RF antenna to generate the plasma, while the total discharge pressure was set at $p = 1.0$ Pa.

B. OES measurement

The line-of-sight k dependence of the spectral radiance on the air side surface of the view window, $L_k'(\lambda)$, along the line-of-sight was measured using a lens (CLA-SMA2, B&W Tek), an optical fiber (FPC-600-0.2-1.0-SRUV, B&W Tek; core diameter = 600 μm, NA = 0.22), and a spectrometer (MS3504i, SOL instruments) with the charge coupled device (CCD) detector (DU420A-OE, Andor Technology). The angle of view (half angle) of the focusing optics is 1.909°, and the beam waist diameter is 4.059 mm. The line-of-sights were set oblique angles to normal of the view window, as shown in Fig. 9 and Table I due to displaced Snell's law, as discussed in Sec. III A. $L_k'(\lambda)$ was measured by scanning the line-of-sight while maintaining the discharge. Note that the spectral radiance of the spectrometer was calibrated using a spectral radiance standard surface, which was realized using a spectral irradiance standard lamp (JPD100V500WCS, Ushio Lighting) and a standard diffuse reflector (SG 3051, SphereOptics).

$L_k'(\lambda)$ was calculated by using Eq. (20). Furthermore, $\varepsilon_k(\lambda)$ on the radial position was calculated as shown in Sec. III D.

On the each position k, the dependence of the excited-level number density on the radius was calculated from the optical emission lines based on the lines listed in Table II. The excited-level density n_{j*} of level $j*$, which is designated by the Racah notation, is expressed based on the spontaneous emission from level $j*$ to level $i*$ as follows:

$$4\pi \int_{j*\rightarrow i*} \varepsilon_{j*\rightarrow i*}(\lambda)\, \mathrm{d}\lambda = h \frac{c}{\lambda(j*,i*)} A(j*,i*)\, \Lambda_{j*,i*}\, n_{j*}, \quad (47)$$

where $\varepsilon_{j*\rightarrow i*}$ is the spectral emission coefficient of the transition from level $j*$ to level $i*$, the integral on the left-hand side is measured over the spectral profile for transition from level $j*$ to level

TABLE II. Optical emission lines for OES measurement.

	Upper level				Lower level				A coefficient
	Vlcek[1]		Racah[19]		Vlcek[1]		Racah[19]		
Ritz wavelength in air $\lambda(j^*,i^*)$ (nm)[19]	Level j	g_j	Level j^*	g_{j*}	Level i	g_i	Level i^*	g_{i*}	$A(j^*,i^*)(\mathrm{s}^{-1})$[19]
750.38	11	1	$4p'[1/2]_0$	1	5	3	$4s'[1/2]_1^\circ$	3	4.50×10^7
763.51	7	20	$4p[3/2]_2$	5	2	5	$4s[3/2]_2^\circ$	5	2.45×10^7
794.81	8	8	$4p'[3/2]_1$	3	4	1	$4s'[1/2]_0^\circ$	1	1.86×10^7
810.37	7	20	$4p[3/2]_1$	3	3	3	$4s[3/2]_1^\circ$	3	2.50×10^7
811.53	7	20	$4p[5/2]_3$	7	2	5	$4s[3/2]_2^\circ$	5	3.30×10^7
826.45	9	3	$4p'[1/2]_1$	3	5	3	$4s'[1/2]_1^\circ$	3	1.53×10^7
840.82	8	8	$4p'[3/2]_2$	5	5	3	$4s'[1/2]_1^\circ$	3	2.23×10^7
842.46	7	20	$4p[5/2]_2$	5	3	3	$4s[3/2]_1^\circ$	3	2.15×10^7
852.14	8	8	$4p'[3/2]_1$	3	5	3	$4s'[1/2]_1^\circ$	3	1.39×10^7
922.45	7	20	$4p[3/2]_2$	5	5	3	$4s'[1/2]_1^\circ$	3	5.00×10^6
978.45	7	20	$4p[5/2]_2$	5	5	3	$4s'[1/2]_1^\circ$	3	1.47×10^6

$i*$, h is the Planck constant, c is the speed of light, $\lambda(j*, i*)$ is the wavelength of the transition from level $j*$ to level $i*$, $A(j*, i*)$ is Einstein's A coefficient of the transition from level $j*$ to level $i*$, and $\Lambda_{j*,i*}$ is the optical escape factor of the transition of level $j*$ to level $i*$. In the Ar CR model, the excitation levels are grouped for excitation states with similar excitation energies; $Lambda_{j*,i*}$ is considered only for transitions to the ground level and is assumed to be optically thin for transitions to excited levels other than the ground level. The number density n_j of excited-level j, which is specified by the Ar CR model, can be expressed as follows:

$$\frac{n_j}{g_j} = \frac{n_{j*}}{g_{j*}}, \tag{48}$$

where g_j is the statistical weight of level j, which is specified by the Ar CR model; g_{j*} is the statistical weight of level $j*$, which is specified by the Racah notation; and level $j*$ belong to the same level j of the Ar CR model. In this study, the reduced population density n_j was calculated by optical emission line spectra.

The Ar CR model[1] was employed to calculate T_e and N_e from the excited-level number densities. The Ar CR model[1] is an excitation-kinetic model that provides a reduced population density distribution n_i/g_i as a function of T_e [electron energy distribution function (EEDF) was assumed to be Maxwellian], N_e, atomic temperature T_a, ion density N_I, and plasma radius r. The rate equation is expressed as

$$\begin{aligned}\frac{dn_i}{dt} = &\sum_{j=i+1}^{65} [-\{C(i,j)N_e n_i + K(i,j)n_1 n_i\}\\
&+ \{F(j,i)N_e n_j + L(j,i)n_1 n_j + A(j,i)\Lambda_{j,i} n_j\}]\\
&+ \sum_{j=1}^{i-1} [\{C(j,i)N_e n_j + K(j,i)n_1 n_j\}\\
&- \{F(i,j)N_e n_j + L(j,i)n_1 n_i + A(i,j)\Lambda_{i,j} n_i\}]\\
&- \{S(i)N_e n_i + V(i)n_1 n_i\}\\
&+ [\{O(i)N_e + W(i)n_1 + R(i)\Lambda_i\}]N_e N_I - [D(i) + B(i)]\\
&(i = 2, 3, \cdots).\end{aligned} \tag{49}$$

In Eq. (49), C and F are electron-collisional excitation and de-excitation rate coefficients, respectively; K and L are atomic-collisional excitation and de-excitation rate coefficients, respectively; A is the radiative transition probability; S and O are atomic-collisional ionization and electron three-body recombination rate coefficients, respectively; V and W are atomic-collisional ionization and atomic three-body recombination rate coefficients, respectively; R is the radiative recombination rate coefficient; B is the rate of generation of metastable Ar_2 molecules; and D is the diffusion loss of the metastable Ar atom. The rate coefficients were calculated using the method of Vlcek.[1] The quasi-stationary approximation $(d/dt = 0)$ of Eq. (49) yields a set of simultaneous equations with T_e and N_e as input variables and n_i as the output variables. T_e and N_e were determined by fitting the n_i/g_i distributions based on OES measurements with the value obtained from the Ar CR model. The objective function f_I of the fitting is as follows:

$$f_I(T_e, N_e) = \sum_{i\in I}\left(\frac{n_{i\mathrm{model}}(T_e, N_e)/g_i}{n_{i\mathrm{OES}}/g_i} - 1\right)^2, \tag{50}$$

where $n_{i\mathrm{model}}(T_e, N_e)/g_i$ is the value of n_i/g_i from the Ar CR model, whereas $n_{i\mathrm{OES}}/g_i$ is the experimental value obtained by OES measurement. T_e and N_e are obtained by fitting minimizing f_I.

In contrast to the previous studies[3] that aimed at diagnosis with a low-wavelength resolution spectrometer, this study aimed at accurate diagnosis based on multiple emission lines obtained with a high-wavelength resolution spectrometer that had a wavelength resolution of 0.22 nm (FWHM). The 11 emission lines listed in Table II were adopted for the diagnosis. The parameters assumed were $T_a = 400$ K and $N_I = N_e$. The plasma column radius for diffusion calculations was assumed to be 96.5 mm, which corresponds to the half value of the inner minimum height of the chamber. The EEDF was assumed to be Maxwellian in nature.

C. Probe measurement

A single Langmuir probe was employed to obtain T_e and N_e for comparison with those obtained from OES-based diagnosis. A tungsten wire tip (Φ1.55 × L0.50 mm) probe was equipped with a push–pull linear shift mechanism, allowing for scanning of the measurement position in the diameter direction of the chamber. T_e was determined from the slope of the current–voltage characteristics, while N_e was determined from the electron saturation current. Note that OES measurements were performed without the probe inserted.

V. RESULTS AND DISCUSSION

Figure 10 shows the measurement results of the spectral reflectance of the inner wall of the chamber (Sec. III).

Above 400 nm, the spectral reflectance increased monotonically. The variation range of spectral reflectance at the same wavelength was up to 19.6% (λ = 750.3–978.6 nm, wavelength range

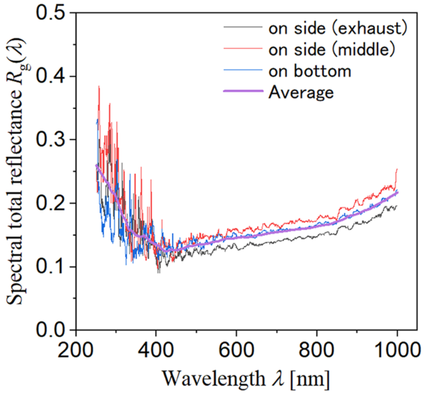

FIG. 10. The spectral reflectance of the inner wall of the chamber: "on side (exhaust)," "on side (middle)," and "on bottom" denote the location of the reflector that was set at side or bottom of the chamber, as shown in Fig. 7. "Average" denotes the averaged and Savitzky–Golay smoothed data of the their spectral reflectance that were employed to calculate the spectral radiance. [This figure was modified from Ref. 20. Reproduced with permission from the work of Yamashita *et al.*, in Proceedings of 43rd International Symposium on Dry Process (DPS2022) (43rd International Symposium on Dry Process Organizing Committee, 2022), pp. 47–48.[20] Copyright 2022 43rd International Symposium on Dry Process Organizing Committee.]

used for diagnosis in this study). Note that the noise observed at the wavelengths below 400 nm is due to the small relative spectral distribution of the incandescent lamp. Note that the reason for the small incremental changes in spectral reflectance on the same curve is considered for the signal-to-noise ratio of the radio-photometric system. Furthermore, the upper part of the chamber of this ICP system had Φ 205 mm quartz window, where the antenna was placed outside the window. Therefore, the light transmitted outside the window was attenuated by multiple reflections. It is assumed that this is a type of light trap behavior, which can be attributed to the low reflectance.

Figures 11 and 12 show the dependence of the spectral emission coefficient, which is the calculation result in Sec. III D based on the experiment. It is clear that by not considering reflections at the wall in this system, the spectral emission coefficient results would result in error, which would be up to 4.1%. In particular, the effect of multiple reflections on the chamber inner wall was found to be significant at locations where the spectral emission coefficient was small. Note that in the spectral radiance calibration setup, which is the same type of this study, the expanded uncertainty (coverage factor $k = 2$) of spectral radiance on the standard surface is reported to be 3.9%–7.4%.[21]

Figure 13 shows the reduced population density distribution, which was calculated from the OES experiment based on Eq. (47).

Figure 14 shows the T_e diagnostic results by OES. The difference between the diagnostic results of T_e with and without reflectance correction was up to 0.6%. Figure 15 shows the N_e diagnostic results by OES. The difference between the diagnostic results of N_e with and without reflectance correction was up to 3.1%.

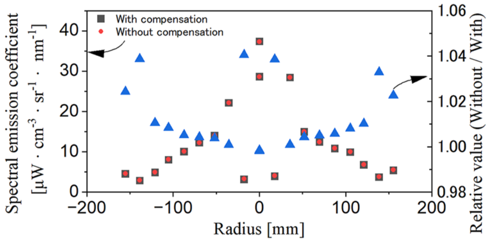

FIG. 11. The dependence of the spectral emission coefficient of 750.4 nm on the position. "With" and "without compensations" denote considering or not the multiple reflectance on the chamber inner wall, respectively.

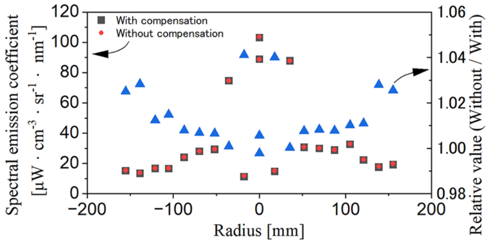

FIG. 12. The dependence of the spectral emission coefficient of 811.2 nm on the position. "With" and "without compensations" denote considering or not the multiple reflectance on the chamber inner wall, respectively.

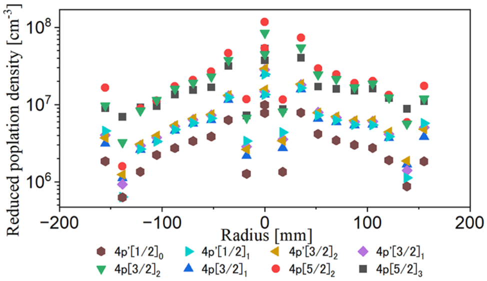

FIG. 13. The dependence of the reduced population density distribution on the position. This result was calculated based on OES measurement with compensation of the reflection on the chamber inner wall.

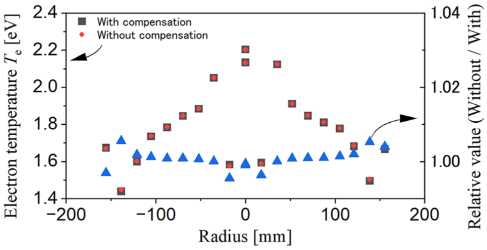

FIG. 14. The diagnostic results of the electron temperature by OES measurement. "With" and "without compensations" denote considering or not the multiple reflectance on the chamber inner wall, respectively.

Figure 16 shows the diagnostic results for the probe. T_e exhibits a convex distribution to position x. The positions of these peaks approximately correspond to the position of the ICP antenna. Meanwhile, N_e exhibited a convex distribution centered at $x = 17$ mm. Both T_e and N_e exhibited asymmetric characteristics because the ends of the ICP antenna on the positive side of the x axis are not perfect spiral-shaped. However, the diagnostic results of the OES and probe measurement differences are ~1 eV for T_e and ten times for N_e, respectively. One of the causes of the difference that is to be considered is the disturbances caused by the insertion of the probe. That is, in this study, the probe was inserted from the port on the x axis positive side wall to the x axis negative side direction. The most part of the probe, except for the tip, is covered by a grounded

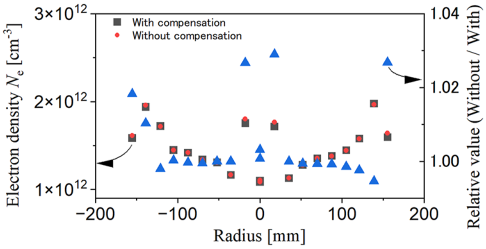

FIG. 15. The diagnostic results of the electron density by OES measurement. "With" and "without compensation" denote considering or not the multiple reflectance on the chamber inner wall, respectively.

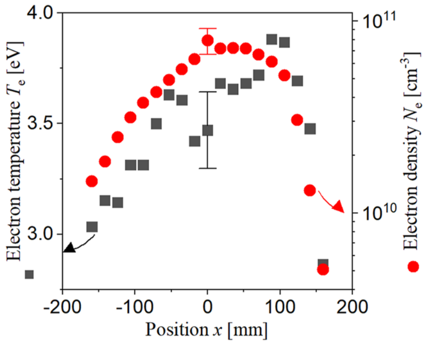

FIG. 16. The diagnostic results of the probe measurement. The error bars denote minimum and maximum values of eight repeated measurements.[20] Reproduced with permission from the work of Yamashita *et al.*, in Proceedings of 43rd International Symposium on Dry Process (DPS2022) (43rd International Symposium on Dry Process Organizing Committee, 2022), pp. 47–48.[20] Copyright 2022 43rd International Symposium on Dry Process Organizing Committee.

stainless steel sleeve. Therefore, the probe insertion affects the electromagnetic field distribution of the plasma. It is reported that the calculated electron temperatures of the probe and OES in a 1 Pa argon inductively coupled plasma differ by about 0.7 eV.[22] Therefore, it is possible that the disturbance was larger on the negative side of the x axis.

The electromagnetic field distribution of the ICP apparatus was simulated with Femtet, Murata Software Co., Ltd. based on the geometric model, as shown in Fig. 17. In the simulation, the electromagnetic field distribution radiated from the antenna was calculated when a high frequency current with an applied frequency of 13.56 MHz and a power of 300 W (the same as in the experiment) was applied to the antenna. For the calculation, the chamber, the antenna shield box, and the quartz window were modeled, as shown in Fig. 17. Note that this simulation assumes a vacuum in the chamber and does not consider space-charge effects.

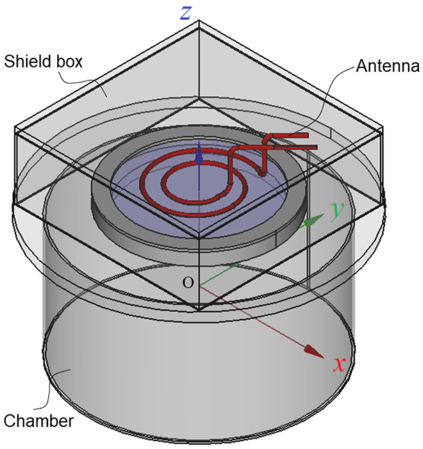

FIG. 17. Geometric model for electromagnetic field simulation of the ICP apparatus. The origin of the coordinate axis is the center of the chamber.

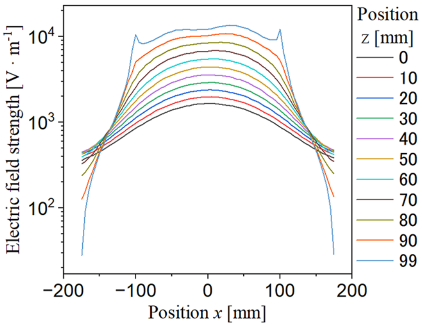

FIG. 18. Electric field strength distribution on the x–z plane at $y = 0$ mm of the ICP apparatus.

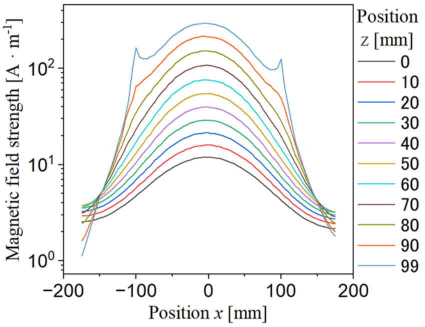

FIG. 19. Magnetic field strength distribution on the x–z plane at $y = 0$ mm of the ICP apparatus.

Figures 18 and 19 show the electromagnetic field strength distributions on the x–z planes at $y = 0$ mm. In the ICP apparatus structure, the quartz window was smaller than the diameter of the discharge chamber, and the window flange, which was grounded, was placed on the inside of the chamber along the diameter. It can be considered that the electromagnetic field is distorted by the grounded flange that entered inward immediately below the quartz window. This is the reason for the formation of the convex spatial electromagnetic field distribution.

Figure 20 shows the electromagnetic field strength distributions on the x–y planes at $z = 99$ mm (directly below the quartz window). Because of the asymmetric shape of the antenna, the electromagnetic field is also asymmetric. This is the cause of the x-directional left-right asymmetry in T_e and N_e, as shown in Figs. 14–16.

Figure 21 shows the horizontal component of the magnetic field strength distributions, which is shown in Fig. 19. The horizontal component of the magnetic field showed an M-shaped magnetic field at $z = 0$.

The study of the electromagnetic field of 13.56 MHz RF ICP in a rectangular chamber was reported by Hopwood *et al.*[23] In their study, a rectangular chamber ($27 \times 27 \times 13$ cm^3) was employed, and a quartz window smaller than the top of the chamber was used, similar to that in the present study. A rectangular spiral antenna was placed outside the quartz window, and a permanent magnet

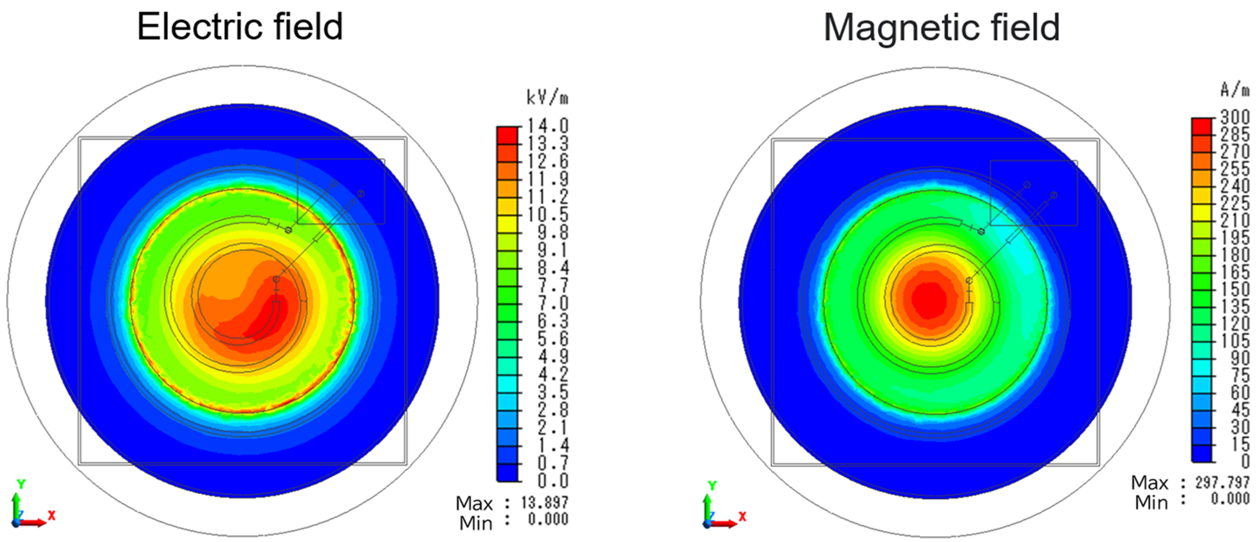

FIG. 20. Electromagnetic field strength distribution on the $z = 99$ mm plane (just below the window) of the ICP apparatus.

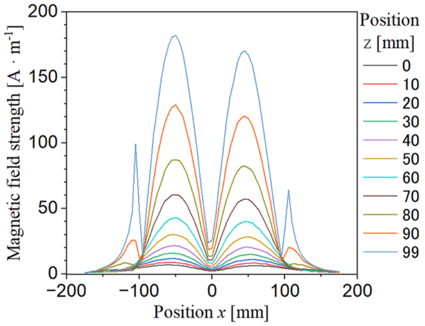

FIG. 21. Horizontal component of the magnetic field strength distribution on the x–z plane at $y = 0$ mm of the ICP apparatus.

for confinement was placed inside the chamber. The result of electromagnetic field calculations and magnetic probe measurements reported an M-shaped magnetic field strength distribution in its horizontal component. It concluded that the magnetic field strength decreased exponentially along the z direction from the antenna because the charged particles absorb power owing to non-collisional heating.

The induced electric field is generated by a high-frequency magnetic field due to Faraday's law. It has been reported that the electromagnetic field caused by the induced electric and magnetic fields induces a drift of $\boldsymbol{v} \times \boldsymbol{B}$ in the electrons,[24] where $\boldsymbol{v}$ is the circumferential component of the velocity of electron. Hence, an electron drift to downstream of the chamber (the negative side of the z axis) will occur. The mean free path of electrons at the pressure in this experiment was estimated to be 39.8 mm. This estimation suggests that fast electrons heated by induced electric field just below the upper quartz window reach the middle of the chamber without much collisions with Ar atoms. Therefore, an convex distribution of electron temperature was observed even at the middle region of the chamber ($z = 0$ mm), while the electromagnetic simulation result shows that convex magnetic field strength distribution only starts below the upper middle window. Therefore, the magnetic field distribution observed just below the upper glass window (Fig. 19) is considered to be observed as an convex distribution of electron temperature because the fast component of the electrons reached even at the center of the chamber ($z = 0$), which is the diagnostic view position.

However, the electromagnetic field simulations in this study did not consider space charge. It is conceivable that the electromagnetic field distribution may change due to space charge. Analysis of gas dynamics in the electromagnetic field, which was not considered in this study, is also a future issue. Other issues are to verify the electron energy distribution function assumed as Maxwell distribution and to elucidate the mechanism of spatial distribution by electromagnetic field analysis considering space-charge effects and gas dynamics.

However, in the present study, both the assumption of uniformity in the z axis direction and the analysis of emission spectroscopy measurements were performed. Therefore, the possibility of differences in diagnostic results due to the z axis position dependence of spectral emission coefficients remains an issue. The diagnosis of three-dimensional spatial distribution by tomographic measurement is a future issue.

VI. CONCLUSION

A method for measuring the spectral reflectance of the inner walls of the chamber was proposed, and its application to the ICP measurement was demonstrated. The effect of the reflected light from the chamber inner wall on OES measurements is discussed. Furthermore, the spectral emission coefficient calculation method was considered with the reflected light from the chamber inner wall. The radial dependence of T_e and N_e was diagnosed by OES measurement based on the proposed method. The Langmuir probe results revealed the effect of the antenna geometry on T_e and N_e. Furthermore, the electromagnetic simulation result suggested that the placement of the antenna and window affected T_e and N_e distribution. The evaluation of the effect of uncertainties in radiophotometry and in the reaction cross section and constants in the collisional radiation model on the electron temperature and electron density is a future issue. Another issue is to elucidate the mechanism of spatial distribution by electromagnetic field analysis considering space-charge effects and gas dynamics. In this study, we assumed axis symmetry, but spectral reflectance correction in tomographic measurements is also a future issue.

ACKNOWLEDGMENTS

This work was supported by JST SPRING, Grant No. JPMJSP2106. This work was the result of promoting public utilization of advanced research infrastructure (program for supporting introduction of the new sharing system), Grant No. JPMXS0420900521.

AUTHOR DECLARATIONS

Conflict of Interest

The authors have no conflicts to disclose.

Author Contributions

Yuya Yamashita: Conceptualization (equal); Data curation (lead); Formal analysis (equal); Funding acquisition (lead); Investigation (equal); Methodology (lead); Software (lead); Visualization (equal); Writing – original draft (lead); Writing – review & editing (equal). **Kenta Doi**: Conceptualization (equal); Formal analysis (equal); Investigation (equal); Visualization (equal); Writing – review & editing (equal). **Tetsuji Kiyota**: Conceptualization (equal); Investigation (supporting); Writing – review & editing (equal). **Keiichiro Asakawa**: Formal analysis (supporting); Investigation (equal); Visualization (supporting). **Sotaro Hosoya**: Formal analysis (equal); Investigation (equal). **Wataru Kikuchi**: Software (supporting); Writing – review & editing (supporting). **Atsushi Nezu**: Investigation (supporting); Resources (lead). **Hiroshi Akatsuka**: Conceptualization (equal); Supervision (lead); Writing – review & editing (equal).

DATA AVAILABILITY

The data that support the findings of this study are available from the corresponding author upon reasonable request.

REFERENCES

[1] J. Vlcek, "A collisional-radiative model applicable to argon discharges over a wide range of conditions. I. Formulation and basic data," J. Phys. D: Appl. Phys. **22**, 623–631 (1989).

[2] Y. Yamashita, T. Akiba, T. Iwanaga, H. Yamaoka, S. Date, and H. Akatsuka, "Developing an optimization algorithm for diagnostic modeling of optical emission spectroscopic measurement of non-equilibrium plasmas based on the argon collisional-radiative model," Jpn. J. Appl. Phys. **60**, 046003 (2021).

[3] Y. Yamashita, T. Akiba, T. Iwanaga, S. Date, H. Yamaoka, and H. Akatsuka, "Optical emission spectroscopic measurement of argon low-pressure inductively coupled plasma based on the optimization algorithm of plasma diagnostic model," IEEE Trans. Plasma Sci. **50**, 1875–1889 (2022).

[4] M. Abdel-Rahman, T. Gans, V. Schulz-von der Gathen, and H. F. Dobele, "Space and time resolved rotational state populations and gas temperatures in an inductively coupled hydrogen RF discharge," Plasma Sources Sci. Technol. **14**, 51–60 (2005).

[5] P. Buchner, H. Schubert, J. Uhlenbusch, M. Weibeta, and K. Willee, "Diagnostics and modelling of a thermal RF plasma process used for the flash evaporation of zirconia powders," Ann. N. Y. Acad. Sci. **891**, 296–303 (1999).

[6] R. Caetano, Y. D. Hoyer, I. M. Barbosa, K. G. Grigorov, and B. N. Sismanoglu, "Radial measurements of gas discharge parameters of atmospheric pressure microplasma," Int. J. Mod. Phys. B **27**, 1350089 (2013).

[7] S. Ries, N. Bibinov, M. Rudolph, J. Schulze, S. Mraz, J. M. Schneider, and P. Awakowicz, "Spatially resolved characterization of a dc magnetron plasma using optical emission spectroscopy," Plasma Sources Sci. Technol. **27**, 094001 (2018).

[8] S. Shi, K. Finch, and G. Gamez, "Radially resolved optical emission spectral imaging study of an atmospheric pressure μDBD jet for elucidating the effect of sample surface material on the underlying mechanisms," J. Anal. At. Spectrom. **36**, 1055–1073 (2021).

[9] S. Shi, K. Finch, Y. She, and G. Gamez, "Development of Abel's inversion method to extract radially resolved optical emission maps from spectral data cubes collected *via* push-broom hyperspectral imaging with sub-pixel shifting sampling," J. Anal. At. Spectrom. **35**, 117–125 (2020).

[10] Q. Xiong, L. Xu, L. Xiong, Q. Huang, Q. Chen, Y. Chen, X. Wang, and X. Jiang, "Heat deposition in the thermal field of a micro-glow discharge: Effect of humidity," Plasma Sources Sci. Technol. **27**, 095010 (2018).

[11] Y.-K. Pu, Z.-D. Yu, and Z.-G. Guo, "Effect of wall reflection on the determination of electron temperature by the line-ratio method in inductively coupled plasmas," Phys. Plasmas **12**, 113301 (2005).

[12] M. Odstrčil, J. Mlynář, V. Weinzettl, P. Háček, T. Odstrčil, G. Verdoolaege, M. Berta, T. Szabolics, and A. Bencze, "Plasma tomographic reconstruction from tangentially viewing camera with background subtraction," Rev. Sci. Instrum. **85**, 013509 (2014).

[13] K. Munechika, H. Tsutsui, and S. Tsuji-Iio, "Visible light tomography considering reflection light in a small tokamak device PHiX," Plasma Fusion Res. **16**, 2402033 (2021).

[14] G. Ghosh, "Dispersion-equation coefficients for the refractive index and birefringence of calcite and quartz crystals," Opt. Commun. **163**, 95–102 (1999).

[15] KLA Corporation, Hakumaku-atsu-sokuteino-tameno-quartz-kussetsuritu (quartz refractive index for thin film thickness measurement) (in Japanese).

[16] H. Yatagai, *Kogaku (Optics)* (Asakura Shoten, Tokyo, 2017) (in Japanese).

[17] *Shinpan Hikari no keisoku manual*, edited by Shoumei-gakkai (Nihon-riko-shuppankai, 2022) (in Japanese).

[18] Y. Yamashita, K. Doi, T. Kiyota, A. Kobayashi, S. Hosoya, K. Yoneda, A. Nezu, and H. Akatsuka, "Position dependence diagnosis of electron temperature and density of inductively coupled argon plasma based on Abel inverted optical emission spectroscopic measurement and collisional-radiative model," in *Proceedings of 11th International Conference on Reactive Plasmas (ICRP-11)/75th Annual Gaseous Electronics Conference (GEC2022)* (ICRP-11 / GEC-2022, 2022), pp. 141–142.

[19] A. Kramida, Yu. Ralchenko, J. Reader, and NIST ASD Team, *NIST Atomic Spectra Database* (National Institute of Standards and Technology, Gaithersburg, MD, 2022), available at: https://physics.nist.gov/asd.

[20] Y. Yamashita, K. Doi, T. Kiyota, S. Hosoya, A. Nezu, and H. Akatsuka, "Diagnosis of argon inductively coupled plasma by optical emission spectroscopic measurement with compensation of spectral reflectance on chamber inner wall," in *Proceedings of 43rd International Symposium on Dry Process (DPS2022)* (43rd International Symposium on Dry Process Organizing Committe, 2022), pp. 47–48.

[21] T. Iwanaga, H. Nakamura, M. Ebisawa, and T. Yamamoto, "Development of calibration system for spectral radiance measurement," Bull. Tokyo Metrop.

Ind. Technol. Res. Inst. (5), 34–37 (2010), available at https://dl.ndl.go.jp/pid/9212384/1/1.

[22] J. B. Boffard, R. O. Jung, C. C. Lin, L. E. Aneskavich, and A. E. Wendt, "Optical diagnostics for characterization of electron energy distributions: Argon inductively coupled plasmas," Plasma Sources Sci. Technol. **20**, 055006 (2011).

[23] J. Hopwood, C. R. Guarnieri, S. J. Whitehair, and J. J. Cuomo, "Electromagnetic fields in a radio-frequency induction plasma," J. Vac. Sci. Technol. A **11**, 147–151 (1993).

[24] A. V. Vasenkov and M. J. Kushner, "Angular anisotropy of electron energy distributions in inductively coupled plasmas," J. Appl. Phys. **94**, 5522–5529 (2003).